Journal of Materials Chemistry C

ROYAL SOCIETY OF CHEMISTRY

PAPER

View Article Online
View Journal

Cite this: DOI: 10.1039/d5tc03885e

Targeted fluorescence enhancement of acridones by hydrogen bonding in solution and solid state

Matthias Jantz,[a] David Klaverkamp,[a] Benedikt Bendel,[b] Takin Haj Hassani Sohi,[c] Martin H. Polko,[c] Lennart Bunnemann,[d] Tobias Böhmer,[e] Markus Putscher,[e] Christel M. Marian,[e] Constantin Czekelius,*[d] Vera Vasylyeva,*[c] Markus Suta[b] and Peter Gilch*[a]

Received 31st October 2025,
Accepted 27th March 2026

DOI: 10.1039/d5tc03885e

rsc.li/materials-c

The fluorescence of many aromatic carbonyl compounds is strongly enhanced by protic solvents. Yet, not all applications allow for protic surroundings. Employing steady state and time-resolved spectroscopy it is shown that *N*-methylacridone (NMA) forms a hydrogen-bonded conjugate with urea derivatives (Schreiner's catalyst, SCat). In toluene solution, the hydrogen bonding results in a 9-fold increase of the fluorescence quantum yield. As evidenced by X-ray crystallography, NMA and SCat form a co-crystal featuring a 3-fold increased fluorescence quantum yield. It further exhibits sharper fluorescence bands. By the aid of quantum-chemical computations, the increased fluorescence quantum yields are attributed to an energetic up-shift of nπ* states.

Introduction

Luminescence is a key property of many biologically or technologically relevant organic compounds. Following photoexcitation, charge recombination, or chemiexcitation, light is emitted as fluorescence or phosphorescence depending on the corresponding spin states.[1] Examples include the green fluorescent protein (GFP),[2–6] flavin mononucleotide binding proteins (FbFP),[7–14] dyes which are used in fluorescence microscopy[15–21] or OLED displays.[22–29] Herein, the overall application efficiency depends on luminescence quantum yields and decay times, color purity, and potential degradation pathways that affect the long-time durability of a dye.[30] Therefore, for optimization, the photophysical characterization of these compounds is of utmost importance and commonly relies on the measurement of temperature-dependent steady-state and time-resolved absorption and emission spectra.[31] These measurements typically employ homogeneous, very dilute solutions in suitable solvents for highest isotropy and minimal artefacts such as aggregation-induced phenomena.[32,33] This way, modification and fine-tuning of the electronic situation in a molecule by suitable substituents can be investigated with high precision and compared with high-level quantum chemical calculations on an isolated chromophore.[34,35] However, surprises are very often encountered when such optimized candidates are put to the test in the actual application or device.[36–39] For example, pure polar or non-polar solvents rarely mimic the situation of a dye in a solid matrix used in OLEDs.[24,30,40–48] Likewise, binding of a luminescent molecule in a protein is mediated by numerous non-covalent interactions, among which hydrogen bonding plays the most pivotal role.[49–67] This directed interaction has two effects in general. First, the energy of all molecular orbitals with non-negligible contributions from atomic orbitals at the corresponding hydrogen bond donor or acceptor is substantially altered. For example, aromatic carbonyl compounds feature dark nπ* transitions which have a huge impact on their fluorescence quantum yields.[68] Population of nπ* states that are energetically accessible from a bright $^1\pi\pi^*$ state usually results in small fluorescence quantum yields. Hydrogen bonding to the oxygen atom of the carbonyl moiety can energetically lift the nπ* states and thereby increase the fluorescence

[a] Institut für Physikalische Chemie, Mathematisch-Naturwissenschaftliche Fakultät, Heinrich-Heine-Universität Düsseldorf, Universitätsstr. 1, 40225 Düsseldorf, Germany. E-mail: gilch@hhu.de
[b] Anorganische Photoaktive Materialien, Institut für Anorganische Chemie und Strukturchemie, Mathematisch-Naturwissenschaftliche Fakultät, Heinrich-Heine-Universität Düsseldorf, Universitätsstr. 1, 40225 Düsseldorf, Germany
[c] Molecular Crystal Engineering, Institut für Anorganische Chemie und Strukturchemie, Mathematisch-Naturwissenschaftliche Fakultät, Heinrich-Heine-Universität Düsseldorf, Universitätsstr. 1, 40225 Düsseldorf, Germany. E-mail: vera.vasylyeva-shor@hhu.de
[d] Institut für Organische Chemie und Makromolekulare Chemie, Mathematisch-Naturwissenschaftliche Fakultät, Heinrich-Heine-Universität Düsseldorf, Universitätsstr. 1, 40225 Düsseldorf, Germany. E-mail: constantin.czekelius@hhu.de
[e] Institut für Theoretische Chemie und Computerchemie, Mathematisch-Naturwissenschaftliche Fakultät, Heinrich-Heine-Universität Düsseldorf, Universitätsstr. 1, 40225 Düsseldorf, Germany

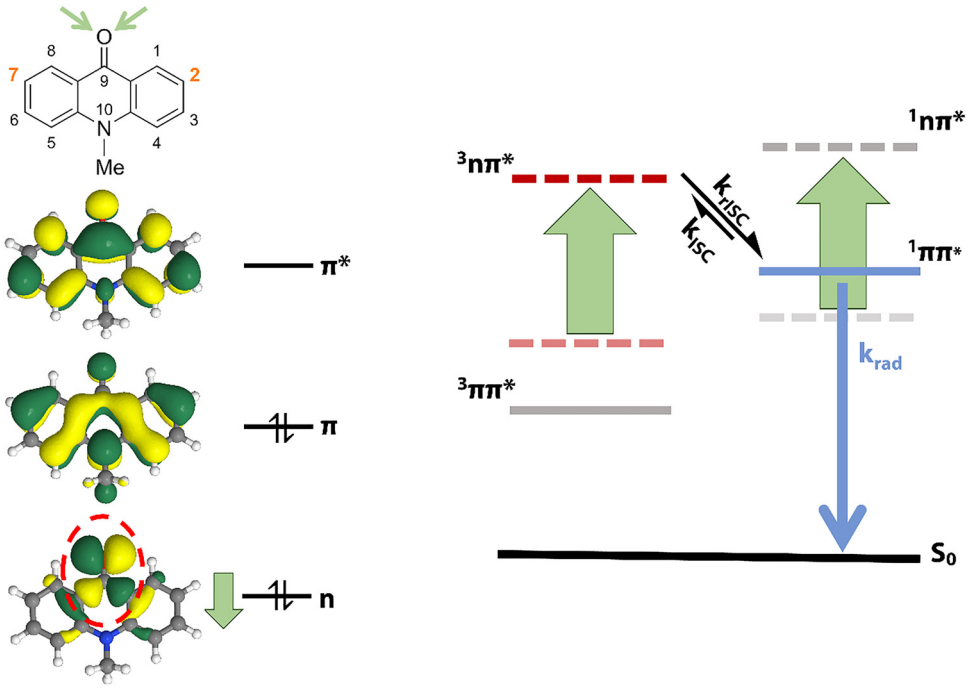

Fig. 1 Illustration of the expected impact of hydrogen bond donors at the carbonyl moiety on the NMA excitation energies. The depiction of the molecular orbitals on the left (adapted from ref. 72) indicates that the n orbital (encircled in red) is predominately affected by hydrogen bonds.

quantum yield by orders of magnitude (Fig. 1). Second, hydrogen bonding of a dye in the solid state can reduce or modulate chromophore–chromophore interactions and thereby suppress undesired spectral broadenings and quenching effects.[69–71]

In this contribution, we present a study aiming at an in-depth understanding on the impact of hydrogen bonding on the luminescence properties of acridones (to avoid hydrogen bond donation by the acridone itself, *N*-methylacridone (NMA) is studied here). NMA behaves like a "prototypical" aromatic carbonyl compound. Its fluorescence quantum yield ϕ_{fl} is strongly solvent-dependent and peaks in protic solvents.[73] The yields approximately increase with the strength of hydrogen bond donor. The importance of hydrogen bonding for this effect was underscored by experiments on acridone water clusters in the gas phase.[74] The addition of only one water molecule boosts the fluorescence quantum yield ϕ_{fl} by two orders of magnitude. Notably, absorption and fluorescence of NMA exhibit only weak solvatochromism[75] which is in line with the local character of the bright ππ* excitation (see molecular orbitals in Fig. 1), in strong contrast to chromophores with charge transfer excitations (see *e.g.* ref. 76). Under suitable conditions, acridones undergo reverse intersystem crossing (rISC) from a higher triplet state ($T_{n\geq 2}$) to the bright ^{1}ππ* one (Fig. 1).[77,78] This HIGHrISC process is particularly interesting for OLED applications as it can convert triplet excitation generated by electron–hole recombination into fluorescence emission. This way, 100% of electrical energy can be theoretically harvested in contrast to the 25% limit of common fluorescence emitters. For effective HIGHrISC, the $T_{n\geq 2}$ state should be slightly higher in energy than the ^{1}ππ* state. As previously shown by some of us, this can be achieved by the attachment of +M substituents at positions 2 and 7 (Fig. 1, highlighted in orange) which lower the ^{1}ππ* state energy.[77,78] In the present study, hydrogen bonding by a urea derivative is shown to increase the fluorescence quantum yield *via* up-shifting nπ* states and simultaneously slightly down-shifting the ππ* states. The approach is operative in solution and solid state. A comparison of the spectroscopic properties of the urea–acridone co-crystal with an acridone crystal reveals reduced chromophore–chromophore interactions in the former. Spectroscopic features as well as X-ray crystallography are corroborated by quantum chemical computations.

Results and discussion

Effect of hydrogen bonding on NMA in solution

Urea derivatives were selected as hydrogen bond donors since they were shown to strongly interact with carbonyl compounds in organocatalysis studies.[79–83] Several urea derivatives (1,3-bis(2-ethylhexyl)urea, 1,3-diphenylurea, and 1,3-bis[3,5-bis(trifluoromethyl)phenyl]urea) (Schreiner's Catalyst, SCat) were tested. SCat showed the most promising results and was, thus, chosen for this study.

To investigate the impact of SCat on the absorption and emission properties of NMA in solution, we conducted a titration experiment in the aprotic, non-polar solvent toluene. The total concentration of NMA (free and bound) was kept constant while the total concentration of SCat was increased between the measurements. NMA is expected to form a hydrogen bond to

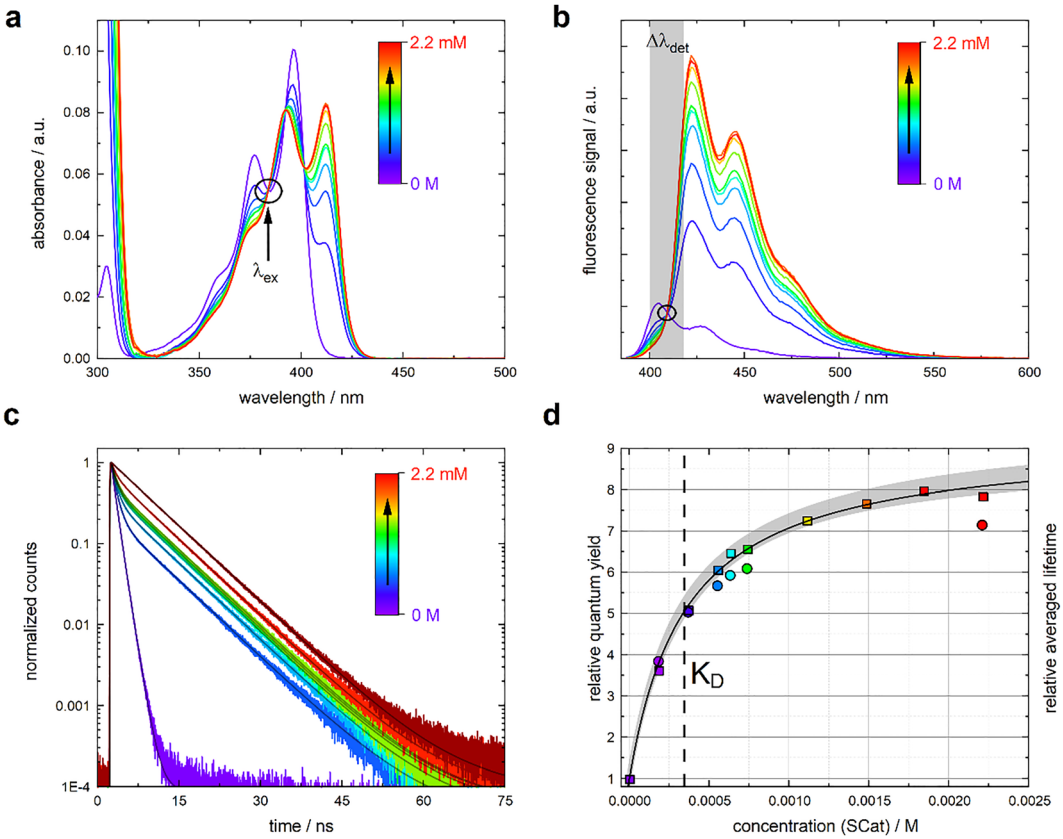

Fig. 2 Influence of the addition of SCat on the absorption and emission of NMA (9.3 μM) in areated toluene. The different SCat concentrations are color-coded from purple (0 mM) to red (2.2 mM). Steady state absorption (a) and emission spectra (b) of NMA are plotted for various SCat concentrations. The excitation wavelength (λ_{ex}) at the isosbestic point at 373 nm is highlighted. The emission spectra were recorded with an excitation and emission bandpass of 1 nm. Fluorescence decay traces (c) for excitation at 383 nm (colored) and 412 nm (2.2 mM SCat, dark red). The detection bandpass ($\Delta\lambda_{det}$) centered at 410 nm is highlighted with a grey rectangle in the emission spectra. The solid lines represent the fits. Relative quantum yields (squares) and relative averaged lifetimes (circles) *versus* the SCat concentration (d). The increase in the relative quantum yield is fitted with a 1 : 1 binding model.[88,89] The grey area around the fit shows the 0.95 confidence band. The fitted K_D value (K_D = 3.46 × 10^{-4} M) is marked with a black, dashed line.

SCat and according to the law of mass action, the fraction of coordinated NMA ought to increase with the total SCat concentration (eqn (S3)). In the absence of SCat, NMA dissolved in toluene absorbs in the near ultraviolet range. The absorption band lowest in energy shows a pronounced vibronic progression with peaks at 396 nm and 378 nm and a shoulder at 358 nm (Fig. 2a, purple). The absorption coefficient maximum is ε = (10 831 ± 169) M^{-1} cm^{-1} for the longest wavelength vibronic peak. The corresponding emission occurs in the range from ~375 nm to 525 nm with maxima at 406 nm, 427 nm and a shoulder at 462 nm displaying a mirror image-type relation to the respective absorption band.[84] A 0-0 energy of around 3.10 eV (25 000 cm^{-1}) and a Stokes shift of only 0.077 eV (620 cm^{-1}) can be derived. The observation of a vibronic fine structure in both the absorption and emission bands as well as the very low Stokes shift are related to the rigidity of the acridone molecules. With the Strickler–Berg approach,[85,86] a radiative rate constant k_r for NMA of 7.79 × 10^7 s^{-1} was derived from the spectra. The fluorescence quantum yield of NMA in toluene was measured using coumarin 102 (ϕ_{fl} = 0.764 in air-saturated ethanol)[87] as a reference. Yields of ϕ_{fl} = 0.063 ± 0.01 and 0.061 ± 0.01 in deoxygenized and air-saturated solutions were obtained. *Via* the partial ground state recovery in a femtosecond transient absorption experiment (Fig. S2 and S3), the triplet quantum yield ϕ_T of NMA was determined to be ~0.9.

When SCat is added to the NMA solution, differences in the absorption spectrum become clearly visible. A new absorption at 412 nm rises with increasing SCat concentration while the absorption peaks below 400 nm concomitantly decrease (Fig. 2a). Isosbestic points at 383 nm, 391 nm, and 401 nm are detected. This observation indicates that two distinct species are present. Clear differences in the emission spectra also become visible with increasing SCat concentration. The emission maximum undergoes a bathochromic shift from 405 nm to 422 nm (Fig. 2b). In addition, the vibrational progression becomes more pronounced. The coordinated form features a 0-0 energy of 2.98 eV (~24 000 cm^{-1}) and a Stokes shift of 0.086 eV (~690 cm^{-1}). For each SCat concentration, a fluorescence spectrum was recorded and referenced to the spectrum of the native NMA. These referenced integrals were then plotted *versus* the corresponding concentration of added SCat (Fig. 2d, squares). The result shows that for the highest addition of SCat,

an enhancement in fluorescence quantum yield by a factor of ~8 was observed. We contribute this to the formation of a hydrogen bonded NMA···SCat complex. This was corroborated by a ^{1}H-NMR experiment (Fig. S6). The fluorescence titration data was fitted with a 1:1 binding model[88,89] (eqn (S4)). This model is in very good agreement with the obtained data and provides a dissociation constant K_D = (3.46 ± 0.31) × 10^{-4} M as well as an increase in the fluorescence quantum yield ϕ_{fl} by a factor of 9.20 ± 0.17 for the fully coordinated NMA (*i.e.* extrapolated to infinite SCat concentration). This K_D value translates into a standard Gibbs free energy ΔG^0_D for the dissociation of (19.8 ± 0.2) kJ mol^{-1}. Involving the molar volume of the contact pair (for details see SI) the enthalpic contribution ΔH^0_D can be estimated to be 22.6 kJ mol^{-1}. As nominally two hydrogen bonds form, the average enthalpy change per bond amounts to 11.3 kJ mol^{-1}. This is in the expected range for dissociation energies of hydrogen bonds (8–167 kJ mol^{-1}).[90]

The fluorescence decay of NMA in the absence of SCat was fitted with a triexponential trial function and allows to determine an average (amplitude-weighted) decay time of 0.87 ns. There are two major components of ~700 ps (relative amplitude of 0.6) and ~1.1 ns (amplitude of 0.4). The third component exhibits a decay time above 10 ns with a very low amplitude of 0.0001. Since the fluorescence of NMA features single-exponential decays in other solvents, *e.g.* THF,[78] this behavior was further investigated using frequency- and time-resolved emission spectroscopy. The obtained decay-associated spectra (DAS) for the two major components are very similar to each other and to the steady state spectrum (Fig. S5). Compared to the steady-state spectrum, the one obtained for the short decay time (~700 ps) is not shifted while the one obtained for the longer decay time is slightly broadened and bathochromically shifted by 0.022 eV (~180 cm^{-1}). Their similarity indicates that the two contributions originate from similar electronic structures. The DAS for the longest decay component (~10 ns) features a different spectral pattern which is significantly bathochromically shifted by 0.294 eV (~2370 cm^{-1}) (Fig. S5). We tentatively assign this component to either NMA excimers or impurities. However, due to its small amplitude, it does not substantially contribute to the overall fluorescence signal.

When SCat is added to the NMA solution an additional decay component of ~6.9 ns arises. The amplitude of this component rises with increasing SCat concentration (Fig. 2c and Table S1). Exciting the solution with the highest SCat concentration at 412 nm (at that wavelength the coordinated form absorbs almost exclusively, Fig. 2a), a nearly single-exponential decay with a time constant of ~6.9 ns is observed (Fig. 2c, dark red). Therefore, we assign the longer decay component to the coordinated form and the shorter ones to free NMA. These shorter time constants slightly depend on the SCat concentration. They increase from 0.71 to 0.76 ns and from 1.09 to 1.53 ns. In the time-resolved measurement, the detection bandpass covers different fractions of the fluorescence spectra of the free and coordinated form (Fig. S1). This leads to an underrepresentation of the amplitude of the long-lived species. Thus, a correction factor must be introduced (eqn (S9)). A plot of the corrected, relative (to the one in absence of SCat), average decay times *versus* concentration (Fig. 2d, circles) reveals that they follow the same trend as the relative fluorescence quantum yields.

To elucidate the impact of hydrogen bonding on the dark states and non-radiative transitions of NMA (not accessible from fluorescence measurements) we performed femtosecond transient absorption (fsTA) measurements on solutions of NMA and NMA···SCat in toluene. As for thioxanthone in methanol[91] and for NMA in THF,[78] a reduction of the stimulated emission (SE) for NMA in toluene with a time constant τ_{eq} of 56 ps is observed (Fig. S4). As discussed in detail in ref. 91, this reduction can be assigned to an equilibration between the $^1\pi\pi^*$ and $^3n\pi^*$ states. The analysis further yields the equilibrium constant $K_{ST} = \frac{[^3n\pi^*]}{[^1\pi\pi^*]}$ of 0.63 which translates into an energy of 0.012 eV (~100 cm^{-1}) by which the $^3n\pi^*$ is above the $^1\pi\pi^*$ one (eqn (S11), (S12) and Fig. S4). For NMA in the presence of SCat, no such reduction was found, which indicates that the $^3n\pi^*$ state is no longer in close energetic proximity (see Discussion). Additionally, no formation of a triplet state was observed in the time window of the measurement (up to 3 ns).

Effect of hydrogen bonding in NMA co-crystals

We demonstrated that the fluorescence quantum yield of acridones can be enhanced *via* hydrogen bond donors in solution. To study the effect in the solid state, co-crystals of NMA and SCat were grown and their crystal structure and photophysical behavior were investigated.

The obtained white bulk micro-crystalline material displays a new X-ray powder pattern, distinctively different from the starting compounds (Fig. 3). A comparison of experimental powder X-ray diffraction (PXRD) pattern with the simulated PXRD from the single-crystal X-ray analysis confirms the targeted NMA···SCat co-crystal phase formation and its purity.

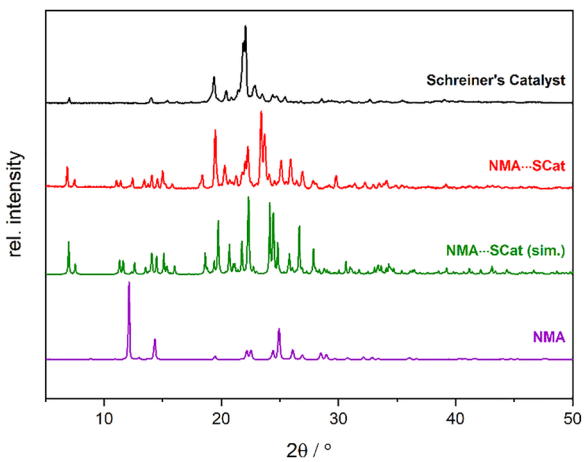

Fig. 3 Comparison of PXRD data of powdered NMA···SCat co-crystals with the starting materials NMA and SCat (CuK$_\alpha$, λ = 1.54059 Å) at 298 K. The simulated PXRD pattern from single crystal structure data acquired at T = 150 K is included. For Rietveld refinement, see SI.

Rietveld analysis of an X-ray powder diffraction pattern of NMA···SCat also showed phase purity of the prepared co-crystalline sample (Table S4 and Fig. S8).

NMA···SCat crystallizes in the triclinic space group $P\bar{1}$ (no. 2) with $Z' = 1$ in a 1 : 1 ratio of the two components. The key intermolecular interaction present in the co-crystal is a bifurcated hydrogen bond between the carbonyl group of NMA and the urea group of the SCat entity (N2–H2···O1: 2.842(2) Å, N3–H3···O1: 2.828(2) Å) (Fig. 4d). Those hydrogen bonds have different lengths indicating slightly asymmetrical concomitance. The described bifurcated N–H···O=C hydrogen bond replaces a comparable interaction present in the SCat structure, also reported here (Fig. S7 and S9).

Viewed along the carbonyl group of NMA, the NMA and SCat units are arranged at a twist angle of 35° (Fig. 4c) which results from the molecular structure of the co-former. The steric hindrance of the SCat ring fragments disallows a co-planar arrangement of both NMA and SCat units. Centroid ring π···π distances of NMA molecules in NMA···SCat are measured to be 4.1366(9) Å, substantially longer than those observed in the pure NMA crystal at 3.6709(13) Å (CCDC Identifier: 1453140, Refcode NMACRO11).[92] It should be noted that the stacking interactions in the NMA crystal structure mentioned above (Refcode NMACRO11) are given as a distance of two geometric centers of the selected aromatic rings which differ from the reported distances of the deposited NMA crystal structure[92,93] where the shortest atomic C···C spacings were measured. In the crystal structure of the chromophore, the NMA molecules are oriented in the same direction and stack just slightly off-set with direct π···π overlay of the aromatic rings. The stacks are closely packed to give a columnar crystal architecture. In contrast, a significant alteration of the stacking arrangement is observed in the NMA···SCat co-crystal. Herein, each two NMA molecules are organized in a parallelly displaced fashion by means of a sandwich-like arrangement giving the shortest π···π distance of over 4 Å. The sandwiches are slipped along the *a* axis to form a NMA ribbon. Those are separated from each other by SCat molecules which are stacked to form 1D columns. These structural features including the formation of hydrogen bonds between NMA and SCat moieties lead to more isolated chromophores in the solid state and weakening of chromophore–chromophore interactions.

IR spectra additionally confirm the formation of the new hydrogen bond in NMA···SCat (Fig. S10). The C=O stretching vibration of NMA shows a redshift by ∼18 cm^{-1}, whereas the originally hydrogen-bonded carbonyl group of pure SCat is distinctively blue-shifted by 54 cm^{-1}, indicating that no hydrogen bond is formed by the urea C=O group in the co-crystal. In fact, in the binary system no strong intermolecular interactions of this moiety are found. Concurrently, the broad N–H stretching vibrations in the co-crystal show similar bathochromic shifts in the 3400–3200 cm^{-1} region. These correlate with the

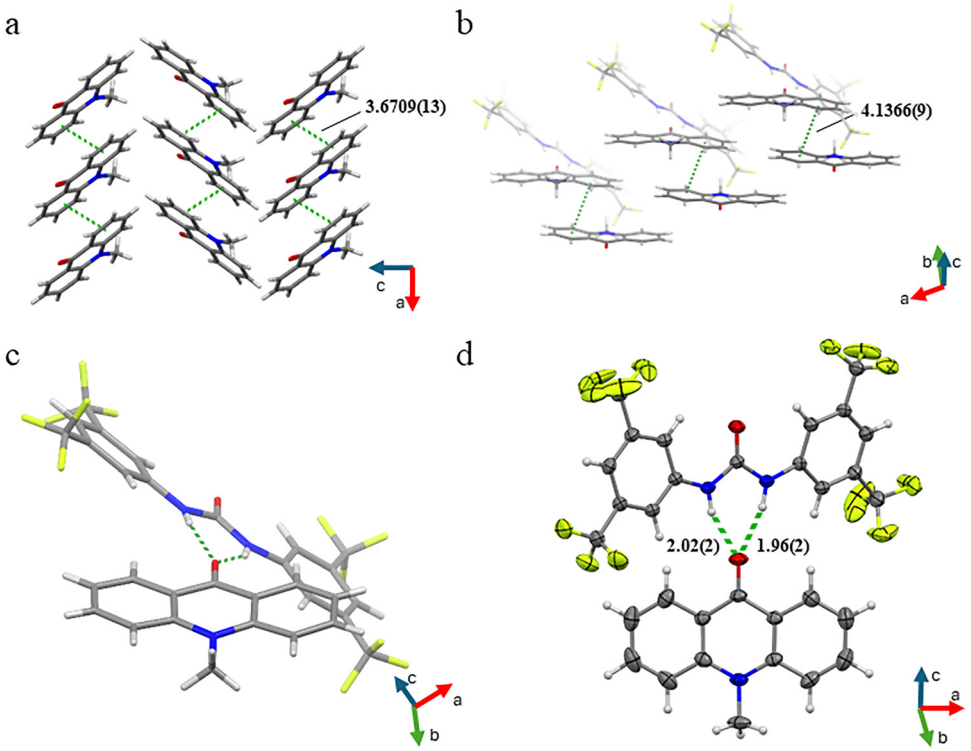

Fig. 4 (a) Crystal packing of NMA (Refcode NMACRO11, CCDC Identifier: 1453140)[92] with herringbone stacking arrangement and $d_{centroid}\cdots d_{centroid}$ of 3.6709(13) Å. (b) NMA···SCat co-crystal with NMA molecules in sandwich arrangement ($d_{centroid}\cdots d_{centroid}$ of 4.1366(9) Å) being parallelly displaced along the *a* axis and slipped along the *c* axis. (c) View at the hydrogen bonded NMA···SCat entity along the *c* axis with a twist angle of 35°. (d) Strong intermolecular N2–H2···O1 (D–H···A 2.02(2) Å, D···A 2.842(2) Å) and N3–H3···O1 (D–H···A 1.96(2) Å, D···A 2.828(2) Å) hydrogen bonds in NMA···SCat co-crystal. Intermolecular interactions and distances are indicated by green dashed lines.

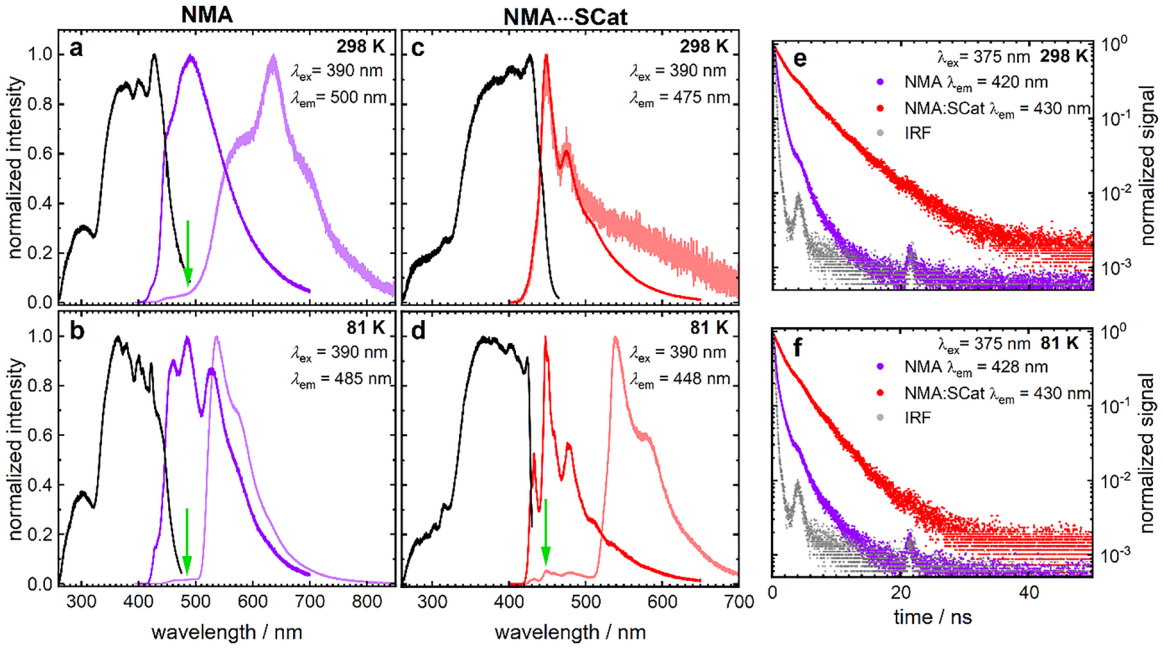

Fig. 5 Excitation (black) and emission spectra of NMA (violet) at 298 K (a) and 81 K (b) and NMA···SCat (red) at 298 K (c) and 81 K (d). The emission after a 1 ms delay is depicted in the corresponding lighter color. The green arrows mark the fluorescence contribution to the late emission. The luminescence decays for NMA and NMA···SCat at 289 K and 81 K are depicted in (e) and (f) respectively. The depicted decays correspond to the shortest measured lifetimes. The resulting lifetimes are depicted in Tables S5–S8. The excitation and emission wavelengths are shown in the corresponding figures.

reported shifts of the vibrational band for similar interaction modes in co-crystalline environment.[94]

To trace the impact of the hydrogen bonding between NMA and SCat on the electronic structure in the solid state, spectroscopic properties of crystalline NMA and NMA···SCat co-crystals were analyzed at different temperatures (T = 81 K and 298 K, Fig. 5). At room temperature, the excitation spectrum of solid NMA upon monitoring the emission at 500 nm shows broadened bands peaking at 427 nm and 303 nm with limited fine structure, which is common for densely packed dyes in solids. Solid NMA strongly emits in the green spectral range with a broad, almost featureless emission band at 492 nm resulting in a Stokes shift of 0.459 eV ($\sim$3700 cm^{-1}) and CIE coordinates[95] of (0.24, 0.36). The absolute fluorescence quantum yield ϕ_{fl} of crystalline NMA was determined to be 0.18 $\pm$ 0.02 (Table 1).

Interestingly, crystalline NMA also displays phosphorescence peaking at 635 nm, which can be detected using time-gated spectroscopy with a 1 ms delay. These observations are in good agreement with earlier reports on the fluorescence and phosphorescence of crystalline NMA.[93] Spectral measurements at T = 81 K reveal a better resolved fine structure in the luminescence spectra. While the spectral position of the fluorescence is barely affected by the temperature decrease, the time-delayed signal shows a strong blueshift upon temperature decrease and the corresponding emission becomes much narrower. The enhanced signal-to-noise ratio at lower temperatures shows that the state responsible for the phosphorescence is less prone to non-radiative decay. Time-resolved photoluminescence studies at 81 K and room temperature confirm that interpretation (Fig. S12 and Tables S9, S10).

The excitation spectra of co-crystallized NMA···SCat have a similar appearance as the respective spectra in solid-state NMA and are broad and featureless (Fig. 5 and Fig. S13). In contrast, the emission spectra of the co-crystal reveal crucial differences with respect to the NMA crystal. Both at room temperature and

Table 1 Spectroscopic properties of NMA and NMA···SCat crystals at 298 K and 81 K. Enclosed are the emission maxima under steady-state conditions (λ_{em}) and after the 1 ms delay ($\lambda_{em,gated}$), the intensity-weighted average lifetime of the fluorescence (τ_{fl}) and phosphorescence (τ_{ph}) at the stated emission wavelength, the absolute fluorescence quantum yield (ϕ_{fl}) and the singlet–triplet energy gap ($\Delta E_{S_1T_1}$)

	NMA		NMA···SCat	
	298 K	81 K	298 K	81 K
λ_{em}/nm	492	484	448	448
$\lambda_{em,gated}$/nm	635	537	448	539
τ_{fl}/ns	1.3 @ 420 nm	1.9 @ 428 nm	4.7 @ 430 nm	3.4 @ 430 nm
τ_{ph}/ms	36.5 @ 635 nm	538.6 @ 535 nm	143.1 @ 448 nm	882.7 @ 540 nm
ϕ_{fl}	0.18 $\pm$ 0.02	—	0.61 $\pm$ 0.02	—
$\Delta E_{S_1T_1}$/eV	0.57 $\pm$ 0.05	0.52 $\pm$ 0.05	—	0.47 $\pm$ 0.05

81 K, the fluorescence bands are hypsochromically shifted (λ_{max} = 448 nm) and are narrower with much more pronounced vibronic fine structure. The CIE coordinates[95] are (0.17, 0.18) at room temperature. The co-crystal spectra share common features with the spectra obtained from dissolved NMA···SCat (Fig. 2). The absolute fluorescence quantum yield of the co-crystal NMA···SCat substantially increases to ϕ_{fl} = 0.61 ± 0.02 compared to the quantum yield of solid NMA (ϕ_{fl} = 0.18 ± 0.02, see above). Also, the longer intensity-weighted average decay times in NMA···SCat (τ = 4.7 ns at room temperature) compared to solid NMA (τ = 1.3 ns at room temperature) confirm these findings. For both samples and temperatures, multi-exponential and wavelength-dependent decay patterns are observed (Fig. S11 and Tables S5–S8) as it is often the case for organic solids.[96,97] From the spectral and temporal properties, it becomes evident that co-crystallization of NMA with SCat has two beneficial effects. On the one hand, it suppresses chromophore–chromophore interactions as evidenced by sharper fluorescence spectra. On the other hand, the co-crystallization with SCat and the subsequent hydrogen bond formation raises the energy of the $^{1,3}n\pi^*$ states and thus limits non-radiative deactivation of the emissive $^1\pi\pi^*$ state by ISC, similar to the findings in solution.

The urea complex formation also impacts the delayed emission of NMA. At room temperature, there is still a substantial contribution in the spectral range of the fluorescence band with an additional shoulder at around 540 nm. That signal may be related to room temperature phosphorescence with a much smaller strength relative to the phosphorescence signal of crystalline NMA. The absolute phosphorescence quantum yield at room temperature could not be measured within achievable measurement accuracy with the integrating sphere and must be very low, in line with a decreased triplet quantum yield ϕ_T. That redshifted emission becomes much more intense upon cooling to T = 81 K. From the maxima of the anticipated fluorescence and phosphorescence bands, singlet–triplet energy gaps of $\Delta E_{S_1T_1}$ = (0.52 ± 0.05) eV (crystalline NMA) and $\Delta E_{S_1T_1}$ = (0.47 ± 0.05) eV (NMA···SCat co-crystal) are estimated, which makes thermally activated delayed fluorescence (TADF) an improbable mechanism for the presence of the fluorescence signal at millisecond delays. According to the crystal structure data, the closest distance between NMA moieties in the NMA···SCat co-crystal is 4.1366 Å (Fig. 4b). A possible explanation for this result is the diffusion of triplet excitons within the solid and subsequent triplet–triplet annihilation (TTA). Similar features can be found in powdered NMA and have been reported by Hamzehpoor *et al.*[93] before. This mechanism seems to be more prominent at room temperature, which implies temperature-dependent exciton diffusion within the solid. Another noteworthy feature is the unusual observation that the average decay times in the ns domain tend to decrease upon cooling from T = 298 K to T = 81 K (Table 1) in the co-crystals. This could be related to a more complex excited state landscape but will require more extensive future investigations that were out of the scope of this work.

Quantum chemistry

To gain an in-depth understanding of the effect of hydrogen bonding to NMA we performed (TD)DFT (geometries) and DFT/MRCI (transition energies) calculations. The effect of the solution surrounding was considered *via* the PCM model. QM/MM calculations were performed to model the crystal environment (Fig. 6). The results of the quantum chemical calculations support and rationalize the experimental findings.

NMA was investigated with and without coordination by Schreiner's catalyst. For NMA in toluene, the computations yield the following sequence of excited states: the lowest excited singlet state is of $^1n\pi^*$ character and features a 0-0 energy of 3.19 eV. The next singlet state lies 0.05 eV higher (at 3.24 eV) and is of $^1\pi\pi^*$ character. Its computed 0-0 energy favourably compares with the experimental value of 3.10 eV. The computed radiative rate constant amounts to $k_r = 7.7 \times 10^7$ s^{-1} which is in excellent agreement with the value derived by the Strickler–Berg analysis of the spectra ($k_r = 7.79 \times 10^7$ s^{-1}). The lowest triplet state ($^3\pi\pi^*$) lies at 2.58 eV ensued by the one ($^3n\pi^*$) at 3.03 eV (Fig. 7). The computed singlet–triplet gap for

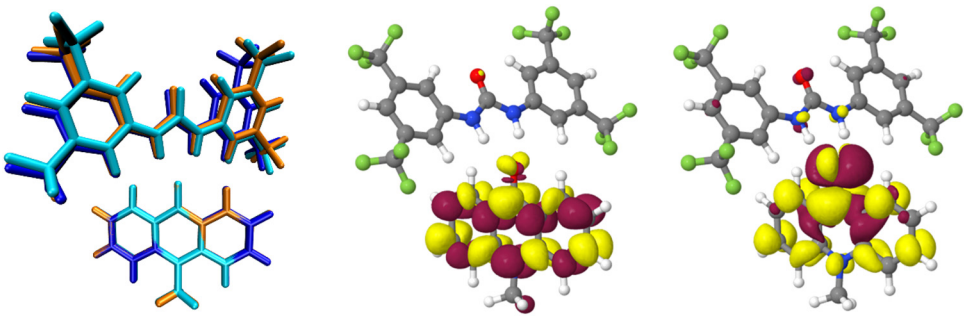

Fig. 6 Left: Overlay of the calculated ground-state geometries of NMA···SCat and its crystal structure [PCM toluene (blue), optimized structure in solid state environment (turquoise) and crystal structure with optimized hydrogen atoms (orange)]. The nuclear frames were aligned to NMA. Difference densities (isovalue = ±0.001, red = decrease of electronic density; yellow = increase of electronic density) for the lowest excited singlet $^1\pi\pi^*$-state (center) and $^1n\pi^*$-state (right) of NMA···SCat. Geometries and difference densities for the corresponding triplet states differ slightly. Only minute contributions of SCat to the energetically lowest electronic excitations can be made out at the optimized excited-state geometries. Molecular orbitals involved in the transitions are displayed in Fig. S15 and S16. Computed at DFT/MRCI-R2016 level of theory [def2-SVP/PBE0/PCM toluene].

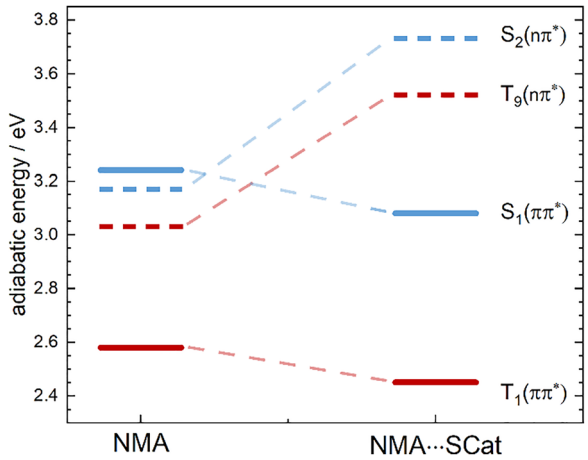

Fig. 7 Comparison of ZPVE-corrected adiabatic energies (0-0 energies) of NMA and NMA···SCat (right) computed at DFT/MRCI-R2016 level of theory [def2-SVP/PBE0/PCM-toluene] highlighting the effect of hydrogen bonding on the lowest excited ππ* (solid lines) and nπ* states (dashed lines) in the singlet (blue) and triplet regime (red). A strong destabilization of the nπ* states and slight stabilization of the ππ* states is visible. For detailed energy schemes, see Fig. S17.

the ππ* states amounts to 0.66 eV, which is close to the value of 0.57 eV (value for NMA crystal). According to the computations, the ^{1,3}nπ* states are slightly lower in 0-0 energy than the ^{1}ππ* state. As elaborated on in a recent study on NMA in THF,[78] such a sequence of excited states is in conflict with a nanosecond fluorescence decay. This leads to the conclusion that the applied quantum chemical approach slightly underestimates the nπ* energies (by ~0.2 eV). Taking this aspect into account, the most likely non-radiative decay path for photo-excited NMA involves an equilibration between the ^{1}ππ* and ^{3}nπ* state within a few tens of picoseconds (Fig. S4). The rapid equilibration is in line with the El-Sayed-allowed character of the transition. The time constant for the equilibration is computed relying on the experimentally derived energy gap between the ^{1}ππ* and ^{3}nπ* state (0.012 eV). The computation yielded rate constants for ISC of $k_{ISC} = 1.9 \times 10^{10}$ s^{-1} and for rISC of $k_{rISC} = 2.4 \times 10^{10}$ s^{-1} in the Franck–Condon approximation. *Via* $\tau_{eq} = \frac{1}{k_{ISC} + k_{rISC}}$ these values translate into a time constant τ_{eq} of the equilibration of 23 ps. This is in fair agreement with the experimental value (56 ps). The equilibrated states mostly decay by a ^{3}nπ* → ^{3}ππ* IC transition. Such a pathway explains the high triplet yield of NMA in toluene ($\phi_T \approx 0.9$).

The geometries of the electronic ground state of the NMA···SCat complex were regarded in different computed environments. Fig. 6 (left) and Fig. S14 show overlays of the experimentally determined (X-ray) crystal structure with optimized hydrogen atoms and of the optimized ground state geometries in PCM-simulated toluene and in a QM/MM-simulated crystalline environment. The overlay shows minor changes and only slightly different orientations of hydrogen bond donor and acceptor towards each other.

According to the computations, the two hydrogen bonds between NMA and SCat are moderately strong (BSSE-corrected complexation energy of 44 kJ mol^{-1} including ZPVE corrections at the PBE0/def2-SVP level of theory). A study by Zheng *et al.*[98] already showed that hydrogen bonds formed between carbonyl groups and 1,3-bis(trifluoromethyl)phenyl-substituted ureas and thioureas tend to be the strongest within the combinations of hydrogen bond donor and acceptor that were investigated. The quantum-chemically determined binding energy of 22 kJ mol^{-1} per hydrogen bond can, however, not directly be compared to the value of 11.3 kJ mol^{-1} determined experimentally (see above). For a valid comparison, it has to be noted that SCat (which is added in high concentrations to the solution) forms hydrogen bonds with other SCat molecules that have to be dislodged first before the urea unit can bind to the carbonyl group of NMA. Assuming that SCat forms dimers in toluene solution, similar to the ones observed in the crystalline structure, we obtained a BSSE-corrected complexation energy of 9 kJ mol^{-1} (4.5 kJ mol^{-1} per hydrogen bond) for the SCat dimer. Subtracting this bond-preparation energy from the bond formation energy yields an association energy of about 18 kJ mol^{-1} per H-bond in NMA···SCat. The quantum chemically determined hydrogen bond strength is still larger than the value derived from the dissociation constant in the experiment, but the value is in the right ballpark. The similarity of computed structures in solution and in the crystalline state is in line with similar increases in the fluorescence quantum yields. This also suggests similar effects of the coordination on the excited state energies.

Comparing the 0-0 energies of NMA with and without coordination by SCat (Fig. 7), one can conclude that the formation of hydrogen bonds slightly decreases the energy of the lowest excited ππ* states (by about 0.1 eV). This matches the redshift observed in the titration experiment (0.12 eV, see Fig. 2a and b). The lowest excited nπ* states are strongly destabilized (by about 0.5 eV). In fact, the nπ* states are raised in energy to such a high extent that they are no longer in close energetic proximity of the lowest-lying bright state and should therefore play no role in the excited state deactivation anymore. The up-shift of the ^{3}nπ* state is in line with the absence of an equilibration signature in the fsTA experiment (Fig. S4) and decelerates non-radiative processes now involving an El-Sayed-forbidden ISC process (^{1}ππ* → ^{3}ππ*) and IC to the ground state. Together with the slightly increased radiative rate constant (7.7×10^{7} s^{-1}–9.4×10^{7} s^{-1}), these findings contribute to the rise in fluorescence quantum yield.

Discussion

NMA is a promising emitter for different types of application as in protic solution it features a high fluorescence quantum yield and can convert triplet excitation into light.[99] However, its properties in aprotic solutions[73] (toluene) and in the solid state[93] (crystal) are not optimal since its fluorescence quantum yield ϕ_{fl} is small (ϕ_{fl} = 0.063) and fluorescence lifetime τ_{fl}

(τ_{fl} = 1.3 ns) is short in toluene. This is due to non-radiative deactivation of the $^1\pi\pi^*$ state by ISC to the $^3n\pi^*$ state followed by IC to the lowest triplet state ($^3\pi\pi^*$) resulting in a high triplet yield.[68,77,78] In the NMA crystal the same deactivation pathway seems to be operative as evident by the observation of room temperature TTA and phosphorescence.[93]

To tailor the emission properties both in solution and solid state a hydrogen bond donor in the form of a urea derivative (SCat) was co-dissolved/crystalized. The titration experiment as well as the crystal structure and the quantum chemical calculations clearly indicate that SCat binds to NMA by means of hydrogen bonds. The calculated bond lengths and angles are similar to the ones observed in the crystal structure. Based on the observed D–H···A distances the hydrogen bond can be categorized as moderately strong.[100] This is in line with the titration experiment which yields a hydrogen binding energy of $\sim$23 kJ mol^{-1} (for both bonds, determined *via* the K_D value, see SI). This value is in the same order of magnitude as the one obtained from the quantum chemical calculations (36 kJ mol^{-1} for both bonds).

This work has shown that the fluorescence quantum yield of NMA in solution as well as in solid state can be substantially enhanced by adding urea derivatives such as SCat as a hydrogen bond donor. The addition of SCat raises the energy of the $n\pi^*$ states by almost 0.5 eV and thereby supresses otherwise relevant non-radiative deactivation pathways. This is reflected in an increase of the fluorescence quantum yield ϕ_{fl} by a factor of $\sim$9 in solution and $\sim$3 in the solid state. Besides that, the addition of SCat in the solid state interferes with the stacking of NMA molecules by placing SCat in a sandwich-like arrangement in between the chromophores (Fig. S7). This structural feature increases the centroid ring $\pi\cdots\pi$ distances between NMA molecules from 3.67 to 4.14 Å. This results in more isolated chromophores, shifting the emission towards the deep blue region (450–475 nm) while suppressing spectral broadening of the emission bands. Nonetheless, that closest distance of 4.14 Å is still sufficiently small to allow diffusion of triplet excitons within the co-crystal and the possibility of TTA.

For an OLED emitter, not only a high fluorescence quantum yield $\phi_{fl} \sim 1$ is crucial but also its ability to convert triplet excitons into light. For HIGHrISC to be operative, the $^3n\pi^*$ energy must be slightly above the one of the $^1\pi\pi^*$ state to ensure that the majority of the population resides in the bright S_1 state. According to Fig. 7, this condition is obviously fulfilled. Yet, there are three reasons why the $^3n\pi^*$ state should not be too high in energy. (i) The state energy defines the minimum voltage necessary to drive the device.[101] Higher energies imply higher input voltages and thereby higher losses. (ii) The triplet energies of embedding matrix molecules need to be higher in energy than the $^3n\pi^*$ state. Matrix molecules with such high triplet energies are scarce.[102] (iii) In the NMA···SCat co-crystal, many triplet states and one singlet charge-transfer state are energetically below the relevant $^3n\pi^*$ state. This will presumably mediate IC transitions to the T_1 state out-competing rISC to the S_1 state. A somewhat weaker hydrogen bond donor (*e.g.* without CF_3 groups) should lead to a desired smaller upshift of the $n\pi^*$ states. A weaker hydrogen bond donor will lead to less association in solution but should still be able to form a co-crystal with enhanced fluorescence properties and HIGHrISC behavior. Besides that, the multiple hydrogen bond interactions could be used to induce preferential orientation of the emitters. This results in an increase of the electron and hole mobility[103] as well as a better outcoupling efficiency[104] which are important practical obstacles in the device manufacturing of OLEDs. Consequently, matrix compounds with the ability to form hydrogen bonds with emitters are promising for the rational design of efficient OLEDs with a high color purity.

Experimental and computational methods

Materials

N-Methylacridone (NMA, $\geq$98%, lot no.: PVQUF-0 M) was received from TCI (solution experiments) and from BLDpharm ($\geq$98%, lot no.: CMA435, solid state experiments). 1,3-Bis(3,5-bis(trifluoromethyl)phenyl)urea (SCat, $\geq$98%, lot no.: DLL312) was purchased from BLDpharm. Toluene (p.a., lot no.: 2379234), toluene-d_8 (99.6 atom% D, lot no.: MKCM 3696), and ethanol (HPLC grade, lot no.: I1313427 346) were obtained from Sigma Aldrich. Coumarin 102 was purchased from Radiant Dyes Laser & Acc. All chemicals obtained commercially were used as received. All measurements in solution were performed at room temperature ($\sim$20 °C). To deoxygenate sample solutions, nitrogen (Air Liquide, 99.999%) was bubbled through.

Titration protocol

To keep the total NMA concentration constant during the titration experiment, the following procedure was applied: a stock solution of NMA in toluene ($A_{410nm} \sim 0.05$, $\sim$8 μM) was prepared and split into two fractions. To one of them SCat was added resulting in a concentration of 0.22 mM SCat. The titration was conducted by mixing different volumes of each stock solution.

Synthesis of the crystals

Single crystals of the NMA···SCat co-crystal were synthesized *via* liquid-assisted grinding of equimolar amounts of 5 mg (23.89 μmol) NMA and 11.62 mg (23.99 μmol) SCat with 5 μL methanol and zirconium oxide balls in a Retsch MM400 ball mill at 12 Hz frequency for 10 minutes. Clear, colorless, plate-shaped single crystals were obtained by putting the obtained powder in 5 mL methanol and slowly evaporating the solvent. Bragg reflections 2θ/°: 14.99, 18.39, 19.50, 22.28, 23.41, 23.70, 25.09, 25.92; IR/cm^{-1}: 3315, 3270, 3120, 3018, 1719, 1579, 1554; TGA/°C: 245 (98% mass loss).

Instrumentation

Steady state absorption spectra of solutions were recorded using a Lambda 1050+ spectrometer from PerkinElmer GmbH. Emission spectra of liquid samples were measured in right-angle detection mode with a FluoroMax-4 by Horiba Scientific.

Cuvettes from Hellma Analytics (Art. no. 117100F-10-40 and Art. no. 111-10-40-QS) were used for all measurements. All spectra were corrected for the spectral sensitivity of the instruments. The 0-0 energies and Stokes shifts were determined by converting the fluorescence spectra from a constant wavelength bandpass to a constant wavenumber bandpass through multiplication by λ^2.[105] Moreover, the absorption spectra were multiplied by $\tilde{\nu}^{-1}$ and the fluorescence spectra by $\tilde{\nu}^{-3}$ to convert them into the transition dipole moment representation.[106] The 0-0 energies were determined from the intersection between the absorption and fluorescence spectra in this representation, with both spectra normalized to their respective maxima.

The instrumentation for femtosecond transient absorption spectroscopy has been detailed previously.[107] Therefore, only a brief overview of the parameters relevant to this study is given here. A 1 kHz Ti:Sa laser amplifier system (Coherent Libra), delivering 800 nm pulses with a duration of 120 fs (full width at half maximum, FWHM), served as a pulse source. To generate the pump pulses, the 800 nm laser was frequency-doubled to 400 nm using a beta-barium borate crystal. The pulse energy was set to 1 μJ. The pump beam featured a diameter of 160 μm at the sample position. A white light continuum was generated by focusing a part of the fundamental in an eccentrically moved CaF_2 disc. This was used as the probe (100 μm diameter at the sample position). The relative polarization of both beams was set to the magic angle. The time resolution of the measurements was approximately 150 fs (FWHM of the instrument response function (IRF)). Transient spectra were recorded at 139 time delay settings, spanning from −1 to 1 ps on a linear time scale, and from 1 ps to 3.4 ns on a logarithmic one. For each delay setting, 2000 spectra were recorded, and the data were averaged over four successive delay scans. To eliminate solvent signal contributions and correct for time-zero artifacts, a solvent measurement was conducted. Its signal was subtracted from the one of the solutions after proper scaling.[108] The sample solutions were flown through a silica cell (0.5 mm, custom QX, Hellma Analytics). The excitation volume was continually exchanged with a micro annular gear pump (MZR 4622, HNP Mikrosysteme). All sample solutions were air-saturated. Time constants and decay-associated difference spectra (DADS) were obtained using a global fitting procedure with a multi-exponential trial function convoluted with the IRF (see eqn (1)),[109]

$$\Delta A(\lambda, t) = \mathrm{IRF} \otimes \sum_{i=1}^{n} \Delta A_i(\lambda) \cdot \mathrm{e}^{-\frac{t}{\tau_i}}. \quad (1)$$

The fit yields a DADS $\Delta A_i(\lambda)$ for each time constant τ_i.

Time-correlated single photon counting (TCSPC) of the solutions was performed with a FT 300 spectrometer from Pico Quant. A supercontinuum laser (EXW-12 with a spectral extension unit EXTEND-UV, NKT Photonics) was used as the excitation source. The repetition rate was set to 4.88 MHz. For emission detection a hybrid PMT detector from Pico Quant was used. The IRF (FWHM of ∼100 ps) was recorded using a Ludox HS-30 colloidal silica water suspension (Aldrich). Each sample was excited at 383 nm and the emission was detected at 410 nm. The input and output slit widths were set to 2500–4000 μm, resulting in detection band passes of 13.5–21.6 nm to maintain a consistent pile up rate ≤0.6%. For the sample with the highest SCat concentration an additional measurement with excitation at 412 nm, detection at 425 nm, and slit widths of 800 μm (4.3 nm) was performed. The analysis of the lifetime data was conducted using the ChiSurf software.[110] The IRF was taken into account *via* convolution with a multi-exponential trial function.

Time-resolved emission spectra of the NMA solution were obtained by measuring fluorescence decays at multiple wavelengths (393–525 nm, in 5 nm intervals) using the above-mentioned setup. The excitation wavelength was set to 370 nm and the input and output slit widths were set to 1850 μm, resulting in a detection bandpass of 10 nm. For analyzing the data, a global fit analysis was carried out using multi-exponential decay functions. The finite time resolution was taken into account *via* convolution with a Gaussian (FWHM ∼ 100 ps) representing the IRF.[109] From this analysis time constants (τ_i) and corresponding decay-associated spectra (DAS, $S(\lambda, t)$) were obtained (eqn (2)),

$$S(\lambda, t) = \mathrm{IRF} \otimes \sum_{i=1}^{n} S_i(\lambda) \cdot \mathrm{e}^{-\frac{t}{\tau_i}}. \quad (2)$$

All solid-state luminescence spectra were recorded using a FLS1000 photoluminescence spectrometer from Edinburgh Instruments. It was equipped with a 450 W Xe arc lamp for excitation, double-excitation and emission monochromators in Czerny–Turner configuration and a thermoelectrically cooled (−20 °C) photomultiplier tube PMT-980 (Hamamatsu). Emission spectra were corrected for the grating efficiency and PMT sensitivity. Excitation spectra were additionally corrected with respect to the lamp intensity. Gated PLE and PL spectra, as well as gated luminescence decay measurements in the ms time range were recorded using a 60 W Xe flashlamp (Δτ = 1–2 μs temporal pulse width). For the PLE and PL gated spectra the repetition rate of the flashlamp was 100 Hz. Since no clear 0-0 transitions in the emission spectra could be detected, singlet–triplet energy gaps were estimated from the energy difference of the maxima of the prompt and time-gated/delayed emission spectra. For that purpose, the emission spectra were rescaled on an energy scale by weighting the signals with λ^2 (Jacobian correction).[106] The errors were estimated by one half of the averaged full widths at half maximum of the two emission bands.

Luminescence decay measurements of the solid-state fluorescence were recorded using TCSPC with an EPL-375 laser diode (Edinburgh Instruments, 0.15 mW average output power, 90 ps temporal pulse width) as the excitation source and varying emission wavelength (see SI). The IRF was recorded using barium sulfate ($BaSO_4$, 99.998%, Lot Nr.: R11I025) from Thermo Fischer Scientific. The analysis of the lifetime data was conducted using the ChiSurf software.[110]

The IRF was taken into account *via* convolution with a multi-exponential trial function. The detection mode for all gated luminescence decay measurements was single-photon multi-channel scaling (MCS). The analysis of the lifetime data was conducted using Origin Pro software.[111]

Absolute quantum yields of the luminescence were measured with a BenFlect-coated integrating sphere using the 60 W Xe flashlamp as the excitation source with 370 nm as the excitation wavelength. Temperature-dependent measurements were performed with a THMS600 (Linkam Scientific) temperature cell with an accuracy of ±0.1 °C in the temperature range between −193 °C and 25 °C.

Single crystal data of SCat and NMA···SCat were measured using a Rigaku XtaLAB Synergy-S Diffraction System with Cu-Kα (λ = 1.54184 Å) radiation of a sealed micro-focus X-ray tube and HyPix 6000 photon detector at 149.99(10) K. CrysalisPRO (CrysAlisPRO, Oxford Diffraction/Agilent Technologies UK Ltd, Yarnton, England) performed cell refinement, data collection and data reduction. Structure solution was carried out by ShelXT[112] using intrinsic phasing and data refinement was performed by ShelXL[113] with the software package Olex2.[114] All the non-hydrogen atoms were refined with anisotropic displacement parameters. In NMA···SCat the fluorine atoms at three of the four CF_3-groups are disordered. All the hydrogen atoms were experimentally refined. In the SCat structure (Z' = 2) the fluorine atoms at three of the eight CF_3-groups are disordered. The hydrogen atoms bound to the nitrogen atoms were experimentally refined, all remaining hydrogen atoms were calculated. Further crystallographic details are given in Table S3. Details on SCat single crystals are given in SI. Crystal structure data are deposited in the Cambridge Structural Database with the CCDC no. 2434784 (NMA···SCat) and 2446400 (SCat).

Powder X-Ray diffraction data were obtained with a Rigaku MiniFlex at ambient conditions with Cu-Kα (λ = 1.54059 Å) radiation. Data were collected at $\theta/2\theta$ geometry from 5° to 50° with a step size of 0.01° at 5° min^{-1} speed.

The X-ray powder diffraction data used for Rietveld refinement was acquired with a Malvern Panalytical X'Pert Pro Pananalytical powder diffractometer equipped with a Cu-Kα1 source (λ = 1.5406 Å, Ge(220)-monochromator) in Bragg–Brentano geometry and reflection mode. Rietveld refinement was performed with TOPAS 7.13.[115]

FTIR measurements were performed on a Bruker Tensor 27 FTIR spectrometer with an ATR unit in the range of 4000 cm^{-1} to 550 cm^{-1}.

The CIE coordinates were determined using the respective emission spectra and the ARL Spectral Fitting software.[116]

Thermogravimetric analysis (TGA) was executed on a Netzsch TG 209 F3 Tarsus in the range from 30 °C to 600 °C with a heating rate of 5 K min^{-1} under a synthetic air/nitrogen atmosphere. TG curves are presented in the SI Fig. S18.

Quantum chemical computations

The ground state geometries of all investigated compounds were optimized using the Gaussian 16 program[117] package and DFT at the PBE0[118]/def2-SVP[119] level of theory. TD-DFT was used for the optimization of the excited singlet states. The Tamm–Dancoff approximation was used for the geometry optimization of the excited triplet states. The analytic calculation of harmonic vibrational frequencies was performed using the Gaussian 16 program package. Solvent effects were addressed using the PCM[120] model and the QM/MM[121] approach. The basis set superposition error (BSSE) of the complexation energy was estimated according to the Boys–Bernardi counterpoise correction scheme.[122] Due to technical restrictions, the BSSE estimates do not include solvent effects. For the QM/MM computations the geometric parameters of the unit cell were extracted from the available experimental data. A supercell consisting of 350 aggregates of NMA and Schreiner's catalyst was constructed based on the experimental crystal structure. One aggregate (QM region) was optimized within the vicinity of all other molecules (MM region). Subsequently, the surrounding molecules were exported as point charges and used as an implicit crystal environment for all further calculations.

Vertical and adiabatic excitation energies and optical electronic properties were calculated using the DFT/MRCI[123–126] method. Ten excited states were calculated for each singlet and triplet manifold employing BH-LYP[127]/def2-SVP[119] one-particle functions. The R2016[125] Hamiltonian parametrized for a configuration selection threshold of $0.8E_h$ was used. Spin–orbit coupling calculations in atomic mean-field approximation were performed with the SPOCK package.[128] Vibrationally resolved absorption and emission spectra were computed using the VIBES[129,130] program and the recently implemented VH method.[131] For computing ISC and rISC rate constants with VIBES, the adiabatic Hessian approach was employed.

Author contributions

Conceptualization: C. M. M., C. C., V. V., M. S., P. G. Formal analysis: M. J., D. K. B. B., T. H. H. S., L. B., T. B., M. Pu., C. M. M., M. S. Funding acquisition: M. J., D. K., C. M. M., C. C., M. S., P. G. Investigation: M. J., D. K. B. B., T. H. H. S., M. H. Po., L. B., T. B., M. Pu. Supervision: C. M. M., C. C., V. V., M. S., P. G. Visualization: M. J., B. B., T. H. H. S., L. B., T. B., M. Pu. Writing – original draft: M. J., D. K., T. H. H. S., T. B., C. M. M., C. C., V. V., M. S., P. G. Writing – review and editing: M. J., D. K. B. B., T. H. H. S., M. H. Po., L. B., T. B., M. Pu., C. M. M., C. C., V. V., M. S., P. G.

Conflicts of interest

There are no conflicts to declare.

Data availability

The data that supports the findings of this study are available from the corresponding authors upon reasonable request.

Supplementary information (SI) is available. See DOI: https://doi.org/10.1039/d5tc03885e.

CCDC 2434784 and 2446400 contain the supplementary crystallographic data for this paper.[132a,b]

Acknowledgements

We gratefully acknowledge financial support from the Deutsche Forschungsgemeinschaft (396890929/GRK2482, ''MODISC'' and 440366605). David Klaverkamp and Matthias Jantz are grateful for their Kekulé scholarships donated by the Fonds der Chemischen Industrie. The authors also thank the CeMSA@HHU (Center for Molecular and Structural Analytics @ Heinrich Heine University) for recording the NMR-spectroscopic data and Tom Förster for the acquisition of the absolute quantum yield measurements of the samples with the integrating sphere setup. Markus Suta gratefully acknowledges funding by the ''Young College'' of the North Rhine-Westphalian Academy of Sciences, Humanities, and the Arts. Maximilian Stremel and Duong Pham Thuy are acknowledged for their help in performing the Rietveld refinement on the X-ray powder diffraction pattern of the powdered NMA···SCat co-crystals. We further thank Philipp Seiffert and Nabil Assahub for performing TGA analysis of the samples. Dedicated to the memory of Dr Christian Torres Ziegenbein – pioneer of HIGHrISC research.

References

1 S. Das, A. M. Powe, G. A. Baker, B. Valle, B. El-Zahab, H. O. Sintim, M. Lowry, S. O. Fakayode, M. E. McCarroll and G. Patonay, *Anal. Chem.*, 2012, **84**, 597–625.
2 M. Zimmer, *Chem. Rev.*, 2002, **102**, 759–782.
3 A. Tromans, *Nat. Rev. Mol. Cell Biol.*, 2004, **5**, 865.
4 A. A. Pakhomov and V. I. Martynov, *Chem. Biol.*, 2008, **15**, 755–764.
5 A. Acharya, A. M. Bogdanov, B. L. Grigorenko, K. B. Bravaya, A. V. Nemukhin, K. A. Lukyanov and A. I. Krylov, *Chem. Rev.*, 2017, **117**, 758–795.
6 F. Tian, G. Xu, S. Zhou, S. Chen and D. He, *Analyst*, 2023, **148**, 2882–2891.
7 T. M. Li, J. W. Hook III, H. G. Drickamer and G. Weber, *Biochem.*, 1976, **15**, 3205–3211.
8 P. A. Van den Berg, K. A. Feenstra, A. E. Mark, H. J. Berendsen and A. J. Visser, *J. Phys. Chem. B*, 2002, **106**, 8858–8869.
9 M. D. Davari, B. Kopka, M. Wingen, M. Bocola, T. Drepper, K.-E. Jaeger, U. Schwaneberg and U. Krauss, *J. Phys. Chem. B*, 2016, **120**, 3344–3352.
10 E. Romero, J. R. Gómez Castellanos, G. Gadda, M. W. Fraaije and A. Mattevi, *Chem. Rev.*, 2018, **118**, 1742–1769.
11 S. Ko, H. Jeon, S. Yoon, M. Kyung, H. Yun, J.-H. Na and S. T. Jung, *J. Agric. Food Chem.*, 2020, **68**, 5873–5879.
12 W. Zou, H. N. Nguyen and M. L. Zastrow, *ACS Sens.*, 2022, **7**, 3369–3378.
13 A. Lukacs, P. J. Tonge and S. R. Meech, *Acc. Chem. Res.*, 2022, **55**, 402–414.
14 A. Sharma, P. Verwilst, M. Li, D. Ma, N. Singh, J. Yoo, Y. Kim, Y. Yang, J.-H. Zhu and H. Huang, *Chem. Rev.*, 2024, **124**, 2699–2804.
15 M. Y. Berezin and S. Achilefu, *Chem. Rev.*, 2010, **110**, 2641–2684.
16 P. Sengupta, S. B. Van Engelenburg and J. Lippincott-Schwartz, *Chem. Rev.*, 2014, **114**, 3189–3202.
17 H. M. Kim and B. R. Cho, *Chem. Rev.*, 2015, **115**, 5014–5055.
18 M. Sauer and M. Heilemann, *Chem. Rev.*, 2017, **117**, 7478–7509.
19 H. Li and J. C. Vaughan, *Chem. Rev.*, 2018, **118**, 9412–9454.
20 A. M. Kelley, *Single-Molecule/Entity Spectroscopy*, American Chemical Society, Washington DC, 2023.
21 M. Minoshima, S. I. Reja, R. Hashimoto, K. Iijima and K. Kikuchi, *Chem. Rev.*, 2024, **124**, 6198–6270.
22 H. Sasabe and J. Kido, *Chem. Mater.*, 2011, **23**, 621–630.
23 V. Maria Angela, A. Anjali, D. Harshini and S. Nagarajan, *ACS Appl. Electron. Mater.*, 2021, **3**, 550–573.
24 G. Hong, X. Gan, C. Leonhardt, Z. Zhang, J. Seibert, J. M. Busch and S. Bräse, *Adv. Mater.*, 2021, **33**, 2005630.
25 H. Jiang, P. Tao and W.-Y. Wong, *ACS Mater. Lett.*, 2023, **5**, 822–845.
26 H. Wang, Y. Yuan, Z. Wang and Y. Wang, *ACS Appl. Eng. Mater.*, 2024, **2**, 781–810.
27 P. Li, W. Li, Y. Zhang, P. Zhang, X. Wang, C. Yin and R. Chen, *ACS Mater. Lett.*, 2024, **6**, 1746–1768.
28 J. M. Dos Santos, D. Hall, B. Basumatary, M. Bryden, D. Chen, P. Choudhary, T. Comerford, E. Crovini, A. Danos, J. De, S. Diesing, M. Fatahi, M. Griffin, A. K. Gupta, H. Hafeez, L. Hämmerling, E. Hanover, J. Haug, T. Heil, D. Karthik, S. Kumar, O. Lee, H. Li, F. Lucas, C. F. R. Mackenzie, A. Mariko, T. Matulaitis, F. Millward, Y. Olivier, Q. Qi, I. D. W. Samuel, N. Sharma, C. Si, L. Spierling, P. Sudhakar, D. Sun, E. Tankelevičiūtė, M. Duarte Tonet, J. Wang, T. Wang, S. Wu, Y. Xu, L. Zhang and E. Zysman-Colman, *Chem. Rev.*, 2024, **124**, 13736–14110.
29 L. G. Franca, D. G. Bossanyi, J. Clark and P. L. Dos Santos, *ACS Appl. Opt. Mater.*, 2024, **2**, 2476–2500.
30 A. Monkman, *ACS Appl. Mater. Interfaces*, 2021, **14**, 20463–20467.
31 A. Farokhi, S. Lipinski, L. M. Cavinato, H. Shahroosvand, B. Pashaei, S. Karimi, S. Bellani, F. Bonaccorso and R. D. Costa, *Chem. Soc. Rev.*, 2025, **54**, 266–340.
32 J. B. Birks, *Photophysics of Aromatic Molecules*, Wiley-Interscience, London, 1970.
33 Y. Hong, J. W. Lam and B. Z. Tang, *Chem. Soc. Rev.*, 2011, **40**, 5361–5388.
34 A. Reiffers, C. Torres Ziegenbein, A. Engelhardt, R. Kühnemuth, P. Gilch and C. Czekelius, *Photochem. Photobiol.*, 2018, **94**, 667–676.
35 M. K. Kubitz, W. Haselbach, D. Sretenović, M. Bracker, M. Kleinschmidt, R. Kühnemuth, C. A. M. Seidel, P. Gilch and C. Czekelius, *ChemPhotoChem*, 2023, **7**, e202200334.

36 A. F. Rausch, M. E. Thompson and H. Yersin, *Inorg. Chem.*, 2009, **48**, 1928–1937.
37 J. Gierschner, J. Shi, B. Milián-Medina, D. Roca-Sanjuán, S. Varghese and S. Park, *Adv. Opt. Mater.*, 2021, **9**, 2002251.
38 J.-M. Lee, C. H. Kang, J. S. Yoo, H. W. Hwang, S. Kwang Hong, Y. M. Ha and B.-K. Ju, *Org. Electron.*, 2021, **99**, 106328.
39 G. F. Trindade, S. Sul, J. Kim, R. Havelund, A. Eyres, S. Park, Y. Shin, H. J. Bae, Y. M. Sung and L. Matjacic, *Nat. Commun.*, 2023, **14**, 8066.
40 A. P. Kulkarni, C. J. Tonzola, A. Babel and S. A. Jenekhe, *Chem. Mater.*, 2004, **16**, 4556–4573.
41 C. Zhong, C. Duan, F. Huang, H. Wu and Y. Cao, *Chem. Mater.*, 2011, **23**, 326–340.
42 S. Scholz, D. Kondakov, B. Lussem and K. Leo, *Chem. Rev.*, 2015, **115**, 8449–8503.
43 Y. Im, M. Kim, Y. J. Cho, J.-A. Seo, K. S. Yook and J. Y. Lee, *Chem. Mater.*, 2017, **29**, 1946–1963.
44 J. Freudenberg, D. Jänsch, F. Hinkel and U. H. Bunz, *Chem. Rev.*, 2018, **118**, 5598–5689.
45 M. D. Sylvinson, H.-F. Chen, L. M. Martin, P. J. Saris and M. E. Thompson, *ACS Appl. Mater. Interfaces*, 2019, **11**, 5276–5288.
46 E. Tankelevičiūtė, I. D. Samuel and E. Zysman-Colman, *J. Phys. Chem. Lett.*, 2024, **15**, 1034–1047.
47 Y. Kim, Y. Ham, T. N. Le, H. Yang, J. Lee and M. C. Suh, *ACS Appl. Mater. Interfaces*, 2024, **16**, 31372–31383.
48 P. Govindharaj, A. J. Wierzba, K. Keska, M. A. Kochman, G. Wiosna-Sałyga, A. Kubas, P. Data and M. Lindner, *ACS Appl. Mater. Interfaces*, 2024, **16**, 23654–23667.
49 J. Schmidt, P. Coudron, A. W. Thompson, K. L. Watters and J. T. McFarland, *Biochem.*, 1983, **22**, 76–84.
50 Z. Li and E. A. Meighen, *Biochem.*, 1995, **34**, 15084–15090.
51 M. Tegoni, M. Gervais and A. Desbois, *Biochem.*, 1997, **36**, 8932–8946.
52 M. D. Greaves and V. M. Rotello, *J. Am. Chem. Soc.*, 1997, **119**, 10569–10572.
53 L. J. Druhan and R. P. Swenson, *Biochem.*, 1998, **37**, 9668–9678.
54 N. Mataga, H. Chosrowjan, Y. Shibata, F. Tanaka, Y. Nishina and K. Shiga, *J. Phys. Chem. B*, 2000, **104**, 10667–10677.
55 L. H. Bradley and R. P. Swenson, *Biochem.*, 2001, **40**, 8686–8695.
56 R. Reichenbach-Klinke, M. Kruppa and B. König, *J. Am. Chem. Soc.*, 2002, **124**, 12999–13007.
57 T. A. Murray and R. P. Swenson, *Biochem.*, 2003, **42**, 2307–2316.
58 M. Kasim, H.-C. Chen and R. P. Swenson, *Biochem.*, 2009, **48**, 5131–5141.
59 S. Salzmann, M. R. Silva-Junior, W. Thiel and C. M. Marian, *J. Phys. Chem. B*, 2009, **113**, 15610–15618.
60 L. Kammler and M. van Gastel, *J. Phys. Chem. A*, 2012, **116**, 10090–10098.
61 S. L. Tan, J. M. Kan and R. D. Webster, *J. Phys. Chem. B*, 2013, **117**, 13755–13766.
62 V. Nandwana, I. Samuel, G. Cooke and V. M. Rotello, *Acc. Chem. Res.*, 2013, **46**, 1000–1009.
63 M. G. Khrenova, A. V. Nemukhin and T. Domratcheva, *J. Phys. Chem. B*, 2015, **119**, 5176–5183.
64 D. Hamdane, C. Bou-Nader, D. Cornu, G. Hui-Bon-Hoa and M. Fontecave, *Biochem.*, 2015, **54**, 4354–4364.
65 T. Iwata, D. Nozaki, A. Yamamoto, T. Koyama, Y. Nishina, K. Shiga, S. Tokutomi, M. Unno and H. Kandori, *Biochem.*, 2017, **56**, 3099–3108.
66 S. Ko, B. Hwang, J.-H. Na, J. Lee and S. T. Jung, *J. Agric. Food Chem.*, 2019, **67**, 12037–12043.
67 J. M. Musila and S. E. Rokita, *Biochem.*, 2022, **61**, 703–711.
68 V. Rai-Constapel and C. M. Marian, *RSC Adv.*, 2016, **6**, 18530–18537.
69 B. Chakraborty, C. Sengupta, U. Pal and S. Basu, *Langmuir*, 2020, **36**, 1241–1251.
70 M. Hempe, N. A. Kukhta, A. Danos, A. S. Batsanov, A. P. Monkman and M. R. Bryce, *J. Phys. Chem. Lett.*, 2022, **13**, 8221–8227.
71 Y. Mei, Y. Lan, D. Li, J. Wang, L. Xie, X. Peng, J. Li, D. Liu and S.-J. Su, *Chem. Eng. J.*, 2024, **480**, 148351.
72 J. Meissner, B. Kosper, C. M. Marian and R. Weinkauf, *J. Phys. Chem. A*, 2021, **125**, 8777–8790.
73 M. Siegmund and J. Bendig, *Ber. Bunsenges. Phys. Chem.*, 1978, **82**, 1061–1068.
74 M. Mitsui, Y. Ohshima and O. Kajimoto, *J. Phys. Chem. A*, 2000, **104**, 8660–8670.
75 M. Siegmund and J. Bendig, *Z. Naturforsch., A*, 1980, **35**, 1076–1086.
76 A. Mukhopadhyay, A. K. Mishra, K. Jana and J. N. Moorthy, *J. Photochem. Photobiol., A*, 2017, **347**, 199–208.
77 K. A. Thom, F. Wieser, K. Diestelhorst, A. Reiffers, C. Czekelius, M. Kleinschmidt, M. Bracker, C. M. Marian and P. Gilch, *J. Phys. Chem. Lett.*, 2021, **12**, 5703–5709.
78 M. Jantz, D. Klaverkamp, L. Bunnemann, M. Kleinschmidt, C. Czekelius and P. Gilch, *Phys. Chem. Chem. Phys.*, 2025, **27**, 10444–10455.
79 M. C. Etter and T. W. Panunto, *J. Am. Chem. Soc.*, 1988, **110**, 5896–5897.
80 P. R. Schreiner and A. Wittkopp, *Org. Lett.*, 2002, **4**, 217–220.
81 A. Wittkopp and P. R. Schreiner, *Chem. – Eur. J.*, 2003, **9**, 407–414.
82 P. R. Schreiner, *Chem. Soc. Rev.*, 2003, **32**, 289–296.
83 Z. Zhang and P. R. Schreiner, *Chem. Soc. Rev.*, 2009, **38**, 1187–1198.
84 P. Klán and J. Wirz, *Photochemistry of Organic Compounds*, Wiley and Sons, Hoboken New Jersey, 2009, pp. 25–72.
85 S. Strickler and R. A. Berg, *J. Chem. Phys.*, 1962, **37**, 814.
86 W. W. Parson, *Modern Optical Spectroscopy*, Springer, Berlin, 2007.
87 K. Rurack and M. Spieles, *Anal. Chem.*, 2011, **83**, 1232–1242.
88 K. Hirose, *J. Inclusion Phenom. Macrocyclic Chem.*, 2001, **39**, 193–209.
89 P. Thordarson, *Chem. Soc. Rev.*, 2011, **40**, 1305–1323.

90 T. Steiner, *Angew. Chem., Int. Ed.*, 2002, **41**, 48–76.
91 T. Villnow, G. Ryseck, V. Rai-Constapel, C. Marian and P. Gilch, *J. Phys. Chem. A*, 2014, **118**, 11696–11707.
92 T. Takeda and T. Akutagawa, *Chem. – Eur. J.*, 2016, **22**, 7763–7770.
93 E. Hamzehpoor, C. Ruchlin, Y. Tao, J. E. Ramos-Sanchez, H. M. Titi, G. Cosa and D. F. Perepichka, *J. Phys. Chem. Lett.*, 2021, **12**, 6431–6438.
94 V. Vasylyeva, S. K. Nayak, G. Terraneo, G. Cavallo, P. Metrangolo and G. Resnati, *CrystEngComm*, 2014, **16**, 8102–8105.
95 D. R. W. G. Hunt, in *The Reproduction of Colour*, ed. M. A. Kriss, John Wiley & Sons Ltd, Chichester, West Sussex, 2004, ch. 22, vol. 6, pp. 393–426.
96 H. Nishimura, T. Yamaoka, K. Hattori, A. Matsui and K. Mizuno, *J. Phys. Soc. Jpn.*, 1985, **54**, 4370–4381.
97 B. Manna, R. Ghosh and D. K. Palit, *J. Phys. Chem. C*, 2015, **119**, 10641–10652.
98 W. Zheng, Y. Fu, L. Liu and Q. Guo, *Acta Phys. -Chim. Sin.*, 2007, **23**, 1018–1024.
99 K. A. Thom, PhD Dissertation, Heinrich-Heine-Universität Düsseldorf, 2021.
100 G. A. Jeffrey, *An Introduction to Hydrogen Bonding*, Oxford university press New York, 1997.
101 A. B. Köhler and Heinz, *Electronic Processes in Organic Semiconductors*, Wiley-VCH, Weinheim, 2015, pp. 307–388.
102 F. Rodella, S. Bagnich, E. Duda, T. Meier, J. Kahle, S. Athanasopoulos, A. Köhler and P. Strohriegl, *Front. chem.*, 2020, **8**, 657.
103 X. Liu, J. Li, X. Qiu and Y. Pan, *Front. chem.*, 2022, **10**, 954419.
104 J. Frischeisen, D. Yokoyama, A. Endo, C. Adachi and W. Brütting, *Org. Electron.*, 2011, **12**, 809–817.
105 J. Lakowicz, *Principles of Fluorescence Spectroscopy*, Springer, New York, 2006.
106 G. Angulo, G. Grampp and A. Rosspeintner, *Spectrochim. Acta, Part A*, 2006, **65**, 727–731.
107 S. Fröbel, L. Buschhaus, T. Villnow, O. Weingart and P. Gilch, *Phys. Chem. Chem. Phys.*, 2015, **17**, 376–386.
108 M. Lorenc, M. Ziolek, R. Naskrecki, J. Karolczak, J. Kubicki and A. Maciejewski, *Appl. Phys. B*, 2002, **74**, 19–27.
109 H. Satzger and W. Zinth, *Chem. Phys.*, 2003, **295**, 287–295.
110 T.-O. Peulen, O. Opanasyuk and C. A. Seidel, *J. Phys. Chem. B*, 2017, **121**, 8211–8241.
111 O. Version, OriginLab Corporation, Northampton, MA, USA, 2021, 5, 1–15.
112 G. M. Sheldrick, *Found. Crystallogr.*, 2015, **71**, 3–8.
113 G. M. Sheldrick, *Found. Crystallogr.*, 2008, **64**, 112–122.
114 O. V. Dolomanov, L. J. Bourhis, R. J. Gildea, J. A. Howard and H. Puschmann, *J. Appl. Crystallogr.*, 2009, **42**, 339–341.
115 A. A. Coelho, *J. Appl. Crystallogr.*, 2018, **51**, 210–218.
116 W. R. Roberts, T. N. Rohrabaugh and R. M. O'Donnell, *J. Visualized Exp.*, 2021, **174**, e62425.
117 M. J. Frisch, G. W. Trucks, H. B. Schlegel, G. E. Scuseria, M. A. Robb, J. R. Cheeseman, G. Scalmani, V. Barone, G. A. Petersson, H. Nakatsuji, X. Li, M. Caricato, A. V. Marenich, J. Bloino, B. G. Janesko, R. Gomperts, B. Mennucci, H. P. Hratchian, J. V. Ortiz, A. F. Izmaylov, J. L. Sonnenberg, Williams, F. Ding, F. Lipparini, F. Egidi, J. Goings, B. Peng, A. Petrone, T. Henderson, D. Ranasinghe, V. G. Zakrzewski, J. Gao, N. Rega, G. Zheng, W. Liang, M. Hada, M. Ehara, K. Toyota, R. Fukuda, J. Hasegawa, M. Ishida, T. Nakajima, Y. Honda, O. Kitao, H. Nakai, T. Vreven, K. Throssell, J. A. Montgomery Jr., J. E. Peralta, F. Ogliaro, M. J. Bearpark, J. J. Heyd, E. N. Brothers, K. N. Kudin, V. N. Staroverov, T. A. Keith, R. Kobayashi, J. Normand, K. Raghavachari, A. P. Rendell, J. C. Burant, S. S. Iyengar, J. Tomasi, M. Cossi, J. M. Millam, M. Klene, C. Adamo, R. Cammi, J. W. Ochterski, R. L. Martin, K. Morokuma, O. Farkas, J. B. Foresman and D. J. Fox, *Gaussian 16 Rev. C.01*, Gaussian Inc., Wallingford, CT, 2016.
118 C. Adamo and V. Barone, *J. Chem. Phys.*, 1999, **110**, 6158–6170.
119 F. Weigend and R. Ahlrichs, *Phys. Chem. Chem. Phys.*, 2005, **7**, 3297–3305.
120 E. Cances, B. Mennucci and J. Tomasi, *J. Chem. Phys.*, 1997, **107**, 3032–3041.
121 O. Weingart, A. Nenov, P. Altoè, I. Rivalta, J. Segarra-Martí, I. Dokukina and M. Garavelli, *J. Mol. Model.*, 2018, **24**, 1–30.
122 S. F. Boys and F. Bernardi, *Mol. Phys.*, 1970, **19**, 553–566.
123 S. Grimme and M. Waletzke, *J. Chem. Phys.*, 1999, **111**, 5645–5655.
124 M. Kleinschmidt, C. M. Marian, M. Waletzke and S. Grimme, *J. Chem. Phys.*, 2009, **130**, 044708.
125 I. Lyskov, M. Kleinschmidt and C. M. Marian, *J. Chem. Phys.*, 2016, **144**, 034104.
126 C. M. Marian, A. Heil and M. Kleinschmidt, *Wiley Interdiscip. Rev.: Comput. Mol. Sci.*, 2019, **9**, e1394.
127 A. D. Becke, *J. Chem. Phys.*, 1993, **98**, 1372–1377.
128 M. Kleinschmidt, J. Tatchen and C. M. Marian, *J. Comput. Chem.*, 2002, **23**, 824–833.
129 M. Etinski, V. Rai-Constapel and C. M. Marian, *J. Chem. Phys.*, 2014, **140**, 114104.
130 M. Etinski, J. Tatchen and C. M. Marian, *Phys. Chem. Chem. Phys.*, 2014, **16**, 4740–4751.
131 T. Böhmer, M. Kleinschmidt and C. M. Marian, *J. Chem. Phys.*, 2024, **161**, 094114.
132 (*a*) CCDC 2434784: Experimental Crystal Structure Determination, 2026, DOI: 10.5517/ccdc.csd.cc2mqlfd; (*b*) CCDC 2446400: Experimental Crystal Structure Determination, 2026, DOI: 10.5517/ccdc.csd.cc2n3p4m.

